Full-band envelope-function approach for type-II broken-gap superlattices

Till Andlauer and Peter Vogl
Walter Schottky Institut, Technische Universität München, 85748 Garching, Germany
(Received 20 May 2009; published 10 July 2009)

We present a charge self-consistent mesoscopic electronic-structure method for type-II broken-gap superlattices that is based on the multiband $k \cdot p$ envelope-function method. This scheme avoids the separate classification and occupation of electron and hole states that causes the standard effective-mass theory to fail once conduction- and valence-band states strongly intermix. The computational efficiency of envelope-function methods is maintained. Free or bound charge-carrier redistributions can be taken into account self-consistently. With this method that we term as full-band envelope-function approach, we calculate effective band gaps, effective masses, and optical transition energies of InAs/GaSb superlattices as a function of the layer width. Good agreement with experiment is obtained. We also discuss semiconductor to semimetal transitions in wide layer structures. We find the charge carriers to form a two-dimensional gas of approximately massless Dirac particles at a critical layer width.

DOI: 10.1103/PhysRevB.80.035304 PACS number(s): 71.15.−m, 71.20.−b, 73.21.−b

I. INTRODUCTION

Recently, there has been a revived interest in antimonide materials both for electronic applications due to their high mobility[1] and for optical applications in the THz regime due to their widely tunable band structure.[2–5] In combination with InAs, antimonides can form type-II heterostructures with a broken-gap band alignment. These types of heterostructures are particularly relevant for the development of infrared lasers and infrared detectors.[6–8] When a material has a broken gap, the strong hybridization of conduction and valence bands[9] prevents an unambiguous separation into electron and hole states which makes it difficult to intuitively understand and predict the behavior of these materials.[5,10] Indeed, relatively few theoretical approaches have been developed so far to predict the electronic structure of mesoscopic nanostructures with broken gaps.[8,10–17] Atomistic approaches such as *ab initio*,[11] empirical pseudopotential,[12,13] or tight-binding approaches[14] have been used to investigate formation energies, microscopic interface, and global band-structure effects of intrinsic type-II superlattices. Mesoscopic continuum approaches such as envelope-function methods are generally better suited to predict details of band-edge properties in the meV range, free or bound carrier charge-transfer effects, and effects of external fields in spatially extended nanostructures. Unfortunately, the standard effective-mass theory fails for broken-gap semiconductors since it assumes that all states can be unambiguously assigned to and occupied with either electrons or holes.

One of the first attempts to solve this problem was to perform an effective-mass calculation and occupy the eigenstates with electrons or holes in proportion to their bulk character.[10] Other mesoscopic models consider very narrow layer structures with a positive band gap where the standard effective-mass approach is applicable[8] or invoke single-band models and couple electrons and holes solely via the Poisson equation.[15] Recently, an eight-band $\mathbf{k} \cdot \mathbf{p}$ method has been developed for situations where standard multiband envelope function approaches fail.[16,17] However, this method still assumes that the carrier densities can be separated into electron and hole charge densities. By contrast, atomistic approaches such as empirical pseudopotential methods[12] inherently avoid any unambiguity in the determination of the carrier charge density but they do so at the cost of far higher computational effort and have difficulty in treating long-range charge-transfer effects across interfaces and free-carrier effects.

In the following, we will present a mesoscopic electronic-structure method for broken-gap materials that maintains the efficiency of a continuum approach yet does not depend on an *a priori* classification into electron or hole states. This approach is based on the envelope-function framework but modifies it in such a way that a separation into electrons and holes is avoided altogether. Instead, all eigenstates of the Hamiltonian are occupied with electrons from bottom up to the Fermi energy. The latter is calculated self-consistently. Thus, we stay within the electron picture throughout. This approach merges well-established concepts from microscopic band-structure methods with mesoscopic models. With this procedure, we calculate effective band gaps, in-plane effective masses, and interband transition energies of intrinsic InAs/GaSb superlattices as a function of the layer thickness. We compare our results with experimental data[4,14,18] and find good agreement between theory and experiment. We find a semiconductor-semimetal transition for certain layer thicknesses that has been predicted theoretically before with pseudopotential methods.[12]

The paper is organized as follows. In Sec. II, we present the charge self-consistent band-structure method for broken gap materials. We discuss the individual charge contributions in Sec. III and illustrate the method's capability to embrace broken-gap situations. In Sec. IV, we apply the scheme to InAs/GaSb superlattices of different layer widths and compare with experimental data. Finally, the paper is summarized in Sec. V.

II. METHOD

Broken-gap heterostructures are characterized by the lowest conduction band in one material layer to energetically fall

 ©2009 The American Physical Society

below the highest valence band in an adjacent layer. This leads to a pronounced coupling of bands that needs to be taken into account properly. The standard EFA fails to yield the correct charge density in this case, as will be discussed in more detail in Sec. III. Here, we present a mesoscopic method for the calculation of the excess carrier charge density that accounts for the problem of mixed electron and hole band states and will be called full-band envelope-function approach (FB-EFA).

We consider (001)-oriented laterally homogeneous quantum wells with the growth direction along the z axis. We invoke the multiband $\mathbf{k}\cdot\mathbf{p}$ envelope-function method[19–22] that is solved in a discrete real-space basis, embracing N grid nodes along the z axis. In the lateral directions, the wave vector $\mathbf{k}_\parallel$ remains a good quantum number. The Schrödinger equation can be written schematically in the form

$$\sum_{\mu}[\hat{\mathcal{H}}^{\nu\mu}(z,-i\,\partial/\partial z,\mathbf{k}_\parallel)-e\phi(z)]\Psi_i^{(\mu)}(z,\mathbf{k}_\parallel)=E_i(\mathbf{k}_\parallel)\Psi_i^{(\nu)}(z,\mathbf{k}_\parallel), \tag{1}$$

with Hamiltonian $\hat{\mathcal{H}}$ that has been patched up from the bulk $\mathbf{k}\cdot\mathbf{p}$ Hamiltonians $\hat{\mathcal{H}}_{k\cdot p}(\mathbf{k})$ of each constituent material, and where the growth direction z has been Fourier transformed into real space ($k_z\rightarrow -i\,\partial/\partial z$). All bulk Hamiltonians are assumed to have the same valency and include the same numbers of N_C conduction and N_V valence-band basis states so that the relevant energy spectrum of the superlattice states near the Fermi energy is covered. The indices ν,μ run over $N_T=N_C+N_V$ basis states. The wave functions $\Psi_i^{(\nu)}$ denote the νth component of the ith subband envelope function ($\nu\in\{1,\ldots,N_T\}, i\in\{1,\ldots,N_T N\}$) of the $N_T\cdot N$ dimensional Hamiltonian. The lateral wave vectors $\mathbf{k}_\parallel$ are restricted to the two-dimensional Brillouin zone $\Omega_{\mathrm{BZ}}=8\pi^2/a^2$, where a is the lateral lattice constant. The electrostatic potential $\phi(z)$ is determined via the Poisson equation,

$$\frac{\partial}{\partial z}\varepsilon(z)\frac{\partial}{\partial z}\phi(z)=-\rho(z). \tag{2}$$

Here, $\varepsilon(z)$ denotes a position-dependent dielectric constant and $\rho(z)$ is the excess carrier charge density. The Schrödinger and Poisson equations have to be solved in a self-consistent manner. For the concrete applications in this paper, we use a relativistic eight-band $\mathbf{k}\cdot\mathbf{p}$ envelope-function method ($N_C=2$ and $N_V=6$) that has been described in detail in Ref. 23 and has been implemented into the simulation package NEXTNANO.[24] In this model, strain effects are incorporated via linear band-edge deformation potentials. The material parameters have been taken from Ref. 25.

To explain the method, we first consider an intrinsic superlattice without dopants. Furthermore, we assume to have calculated all $N_T N$ eigenstates across the entire Brillouin zone Ω_{BZ}. In the actual calculations, much fewer eigenstates are needed but this will be discussed below. We occupy all of these eigenstates with electrons according to the Fermi-Dirac statistics. Since the entire crystal must be neutral, each node carries the same amount of positive compensating background charge (since the constituent bulk materials are assumed to have the same valency). Consequently, the excess charge density $\rho(z)=\rho_{\mathrm{FB-EFA}}(z)$ is given by

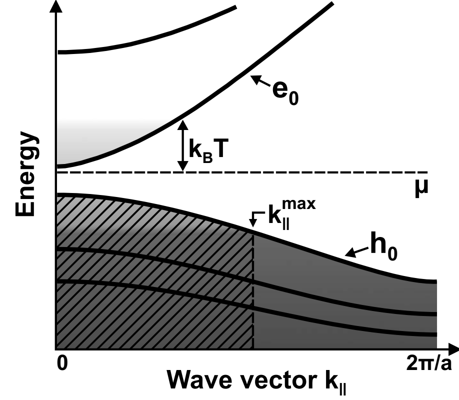

FIG. 1. Schematic subband dispersion and state occupation for a narrow gap superlattice, as a function of the in-plane wave vector $\mathbf{k}_\parallel$. Regions of fully and partly occupied states are marked in dark and light gray, respectively. The shaded region indicates the required amount of background charge density ρ_b, when the k-space integration is restricted to $k_\parallel^{\max}$ as explained in the text.

$$\rho_{\mathrm{FB-EFA}}(z)=e[-n_{\mathrm{FB}}(z)+\rho_b(z)]. \tag{3}$$

In this expression, $n_{\mathrm{FB}}(z)$ is the density of electrons,

$$n_{\mathrm{FB}}(z)=\sum_{i=1}^{N_T N}\frac{1}{(2\pi)^2}\int_{\Omega_{\mathrm{BZ}}}d^2\mathbf{k}_\parallel|\Psi_i(z,\mathbf{k}_\parallel)|^2 f[E_i(\mathbf{k}_\parallel)]. \tag{4}$$

The sum runs over *all* eigenstates of the Hamiltonian and $f(E)$ is the Fermi function. The background charge density $\rho_b(z)$ is given by

$$\rho_b(z)=N_V N\frac{\Omega_{\mathrm{BZ}}}{(2\pi)^2\Delta z}. \tag{5}$$

This density corresponds to the charge of $N_V N$ fully occupied bulk valence subbands. The denominator contains the grid spacing Δz, since the norm of any subband wave function is given by $\|\Psi_i\|=1/\sqrt{\Delta z}$ in the discrete z space. This scheme allows one to easily take into account doping and fixed (e.g., piezoelectric) charges. The only modification required is to add the doping densities of donors (D) and acceptors (A) as well as the fixed charge density ρ_{fixed} to the right-hand side of Eq. (2),

$$\frac{\partial}{\partial z}\varepsilon(z)\frac{\partial}{\partial z}\phi(z)=-\rho(z)+eN_A(z)-eN_D(z)-\rho_{\mathrm{fixed}}(z). \tag{6}$$

It is illustrative to first consider an intrinsic superlattice that has the conventional ordering of electronlike and holelike subbands with a positive band gap. In Fig. 1, we show schematically the energy dispersion of the subbands near the chemical potential μ as a function of the lateral wave vector. According to the conventional EFA, the lowest conduction subband (e_0) gets partly filled with electrons and the highest valence subband (h_0) with holes for low temperatures. In the present FB-EFA, by contrast, we fill all states with electrons from bottom up. According to Eq. (4), the states in the dark

gray areas in Fig. 1 are fully occupied and those in the light gray areas are partly occupied. Note that the light gray valence area is now largely filled with electrons rather than having a minority hole occupation. The excess charge density ρ is obtained by subtracting the background charge density ρ_b from Eq. (5) that corresponds to the shaded area in the figure.

The density in Eq. (4) is integrated over the full two-dimensional Brillouin zone Ω_{BZ}. In a mesoscopic approach, however, only the states close to the center of the Brillouin zone can be accurately calculated. Fortunately, the states exceeding the chemical potential by more than a few k_BT do not contribute to the sum in Eq. (4). Similarly, states that significantly fall below the chemical potential are compensated by the same amount of background charge and do not contribute either. For the concrete broken-gap systems considered in this paper, we find that the wave vectors of partially filled subband states lie within the inner 5–10 % of the Brillouin zone. Thus, we can reduce the maximum wave-vector modulus used in Eq. (4) to a small value $k_{\parallel}^{\max}$, which not only reduces the number of numerical matrix diagonalizations by typically 2 orders of magnitude, but also guarantees that only accurately represented electronic states enter the calculations. This k-space reduction requires an additional adjustment of $\Omega_{\mathrm{BZ}} \rightarrow \Omega_{\mathrm{BZ}}^{*}=4(k_{\parallel}^{\max})^2$ in the relation Eq. (5) for the background charge density.

The computational effort can be further reduced by integrating only over the irreducible wedge Ω_{IW}^{*} of the Brillouin zone that can be obtained by exploiting the symmetry of the lattice.[26] For the cubic zinc-blende quantum wells considered in this paper, Ω_{IW}^{*} covers just 1/8 of Ω_{BZ}^{*}. We have implemented an efficient k-space integration scheme similar to Refs. 27 and 28 that interpolates the probability densities and the energy dispersion between the exactly calculated $\mathbf{k}_{\parallel}$ points. We typically take into account 50 k points within Ω_{IW}^{*}. It turns out that a bilinear interpolation is sufficient for the probability density, whereas higher order schemes are required for the energy dispersion to accurately sample energy minima with a large density of states. In fact, we employ a two-dimensional cubic spline interpolation[29] for the energy dispersion.

Finally, filling up all states with electrons and subtracting a positive background charge is equivalent to filling all states with holes and subtracting an appropriate negative background charge. This is a consequence of the completeness relation of the eigenstates of an Hermitian Hamiltonian. Since the eight-band model includes less bulk conduction bands (N_C=2) than bulk valence bands (N_V=6), the latter approach is computationally more efficient. With this scheme, the density involves only N_CN instead of N_VN states and the number of eigenstates required is only a little larger than N_CN. Nevertheless, we stick to the electron picture in the present discussion to avoid any confusion.

III. DISCUSSION OF METHOD

For the concrete predictions presented in this paper, we consider intrinsic InAs/GaSb (001) superlattices that have been fabricated and studied experimentally.[4,14,18] The structures are characterized by the InAs and GaSb layer widths w_1 and w_2, respectively. The GaSb layers are assumed to be unstrained so that the InAs layers exhibit a slight tensile strain of 0.5%. In Fig. 2, we schematically depict the bulk band edges of the Γ conduction band E_C (dotted line) and the heavy-hole valence band E_V (solid line) for two different regimes of layer widths. The graphs show a type-II broken-gap band alignment with an overlap between E_C in the InAs layer and E_V in the GaSb layer ($E_G<0$). Particularly for small layer widths, it is easy to qualitatively understand the character of the superlattice band-edge states at $k_{\parallel}=0$. Confinement leads to subbands that are derived from the bulk InAs conduction band and lie above E_C, as well as to subbands that are derived from the bulk GaSb heavy-hole band and lie below E_V. In Fig. 2, we show the lowest of the former states (e_0) and the highest of the latter states (h_0).

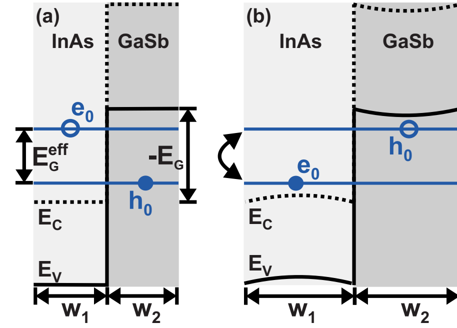

FIG. 2. (Color online) Schematic band structure of InAs/GaSb superlattice with InAs and GaSb layer widths w_1 and w_2, respectively. (a) Sketch of the broken bulk band edges (dashed: conduction bands, full: heavy-hole bands) for narrow layer widths with negative gap E_G in position space. The lowest unoccupied (labeled by e_0) and highest occupied (labeled by h_0) superlattice subbands are also shown and lead to a positive effective band gap E_g^{eff}. (b) Same as in (a) for larger layer widths. The character of the lowest unoccupied and highest occupied subbands is reversed. The effective band gap is still positive but there is a charge transfer between the adjacent layers that leads to a band bending as indicated schematically.

For small layer widths (typically $w_1, w_2 < 9$ nm), the energy difference $E(e_0)-E(h_0)>0$ is positive, leading to a conventional semiconductor.[5,7] This situation is shown in Fig. 2(a). For larger layer widths [Fig. 2(b)], the ordering of InAs and GaSb bulk derived subbands gets switched at $k_{\parallel}=0$ due to the weaker confinement. In such situations, a self-consistent calculation of the Fermi level and consideration of the entire subbands away from $k_{\parallel}=0$ is required to determine the effective band gap, $E_G^{\mathrm{eff}}=E(\mathrm{LU},\mathbf{k}_{\parallel}^{\mathrm{LU}})-E(\mathrm{HO},\mathbf{k}_{\parallel}^{\mathrm{HO}})$, i.e., the energy difference between the minimum of the lowest unoccupied (LU) and the maximum of the highest occupied (HO) subband. As indicated schematically in Fig. 2(b), the mixing of occupied InAs- and GaSb-like states causes a significant amount of charge transfer that leads to band bending.

To investigate this case in more detail, Fig. 3 displays the self-consistent FB-EFA band structure for $w_1=16$ nm and $w_2=8$ nm as a function of the wave vector in the [010] direction together with the energetic position of the Fermi level for zero temperature. This structure is seen to be an indirect-

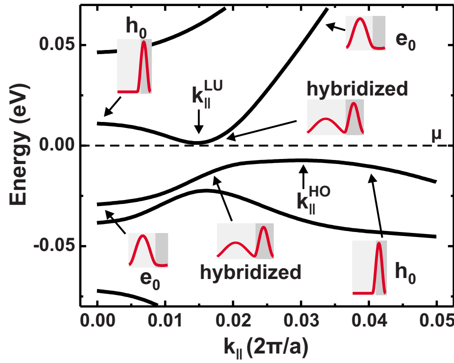

FIG. 3. (Color online) Calculated subband dispersions of an InAs/GaSb superlattice as a function of $\mathbf{k}_{\parallel}$ along the [010] direction. The InAs and GaSb layer widths are 16 and 8 nm, respectively. The lateral lattice constant a is the unstrained GaSb lattice constant. The insets show probability densities of subband eigenstates at different values of $\mathbf{k}_{\parallel}$. The InAs and GaSb layer is indicated by the light and dark gray shading, respectively. All energies are given in meV relative to the chemical potential μ.

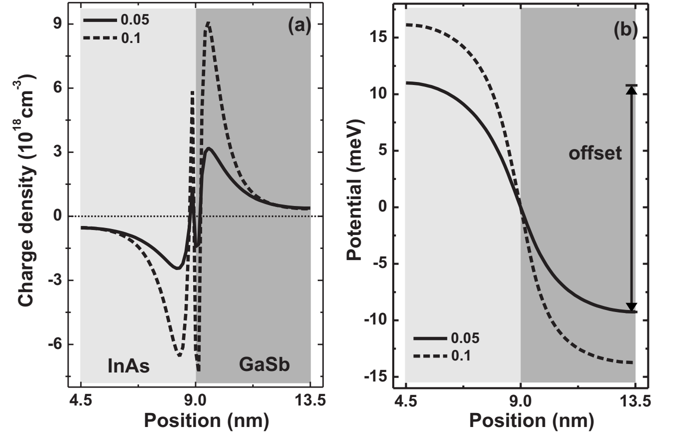

FIG. 4. (a) Calculated local charge densities close to the interface of an intrinsic InAs/GaSb superlattice with equal layer widths of 9 nm. The results are shown for two different values of $k_{\parallel}^{\max}$ (full line: 0.05, dashed line: 0.1 in units of $2\pi/a$). (b) Corresponding potential profile $-e\phi(z)$ for charge density shown in (a). The interface dipoles modify the offset between the band edges.

gap semiconductor on the verge of becoming a semimetal. For small $\mathbf{k}_{\parallel}$ values, the LU (HO) states are almost completely localized within the InAs (GaSb) layer, but for larger $\mathbf{k}_{\parallel}$ values, the characters of these two subbands get switched. Thus, it is not possible to assign the character electronlike or holelike to a complete subband. For intermediate wave vectors, the band structure shows an anticrossing and a strong mixing of electronlike and holelike states. Indeed, the probability distributions of the eigenstates of the two subbands shown in the insets for a $\mathbf{k}_{\parallel}$ point near the anticrossing exhibit two distinct maxima that correspond to an almost equal localization in the InAs and GaSb layers. Obviously, these states cannot be classified as electronlike or holelike and effectively contribute to the electron as well as to the hole charge densities. Thus, it is not possible to simply occupy some subbands according to the Fermi-Dirac statistics of electrons and others with the statistics of holes as it is done in the standard EFA.

We first consider the situation of narrow layer widths that have a standard semiconductor band ordering. Concretely, we consider an intrinsic superlattice characterized by the layer widths $w_1 = w_2 = 9$ nm at $T = 0$ K. In Fig. 4(a), we plot the charge density for the InAs/GaSb superlattice that has been determined within the present FB-EFA method. Here, the coupled eight-band Schrödinger equation [Eq. (1)] and the Poisson equation [Eq. (2)] have been solved iteratively until charge self-consistency is reached. Figure 4(b) depicts the corresponding potential across the interface region.

The resulting charge density exhibits multipoles with a dominant dipolar character very close to the layer interface. These dipoles are produced by the filled valence states whose density is redistributed with respect to the bulk due to the presence of the interfaces. Indeed, such interface dipoles are well known from microscopic first-principles electronic-structure calculations and are one of the sources of the band-edge discontinuities between different materials.[30] In effective-mass theory, the band offsets are input parameters and already take into account the interface dipolar contribution to the total band offset. In this work, we use a value of 510 meV for the valence-band offset.[31] For the present InAs/GaSb interface and taking into account wave vectors up to $k_{\parallel}^{\max} = 0.05 \cdot 2\pi/a$, we obtain a dipole-induced band offset of -20 meV that we compensate by increasing the band offset between InAs and GaSb from Ref. 31 correspondingly. The precise value of this interface dipole depends on the maximal wave vector as shown in Fig. 4. We note that the low-lying valence states that contribute to this small interface dipole are not accurately represented by the present mesoscopic approach. Since we remove the effect of these low-lying states, however, by adjusting the total band offset to its established value, their details do not play a role.

In wide layer superlattices, the strong hybridization of electronlike and holelike states produces additional mesoscopic charge-transfer effects that arise from electronic states close to the Fermi level and are therefore accurately captured by the present FB-EFA method. Concretely, we consider superlattices with $w_1 = 18$ nm and $w_2 = 9$ nm. The charge-density distribution for this case is shown in Fig. 5(a). Since the zone-center HO and LU states are reversed relative to the narrow well situation [see Fig. 2(a)], it is plausible that a charge transfer between the InAs and GaSb layers occurs. Indeed, the charge-density distribution in Fig. 5(a) clearly shows a nonzero net charge density near the centers of the individual layers. Importantly, this density is insensitive to the maximum k value used in the integration in Eq. (4). Altogether, we obtain a charge-density transfer on the order of 10^{18} cm^{-3} between the GaSb and the InAs layers. We note that it is very difficult to resolve such small charge densities in atomistic approaches. The importance of this charge transfer on a mesoscopic length scale can be seen from Fig. 5(b), which shows the band bending induced by the charges transfer. In more detail, this figure depicts the electrostatic potential that corresponds to the density in Fig. 5(a), superimposed on the bulk band edges. This potential shows no dipolar character across the interface due to the extremely small charge associated with the interface dipole.

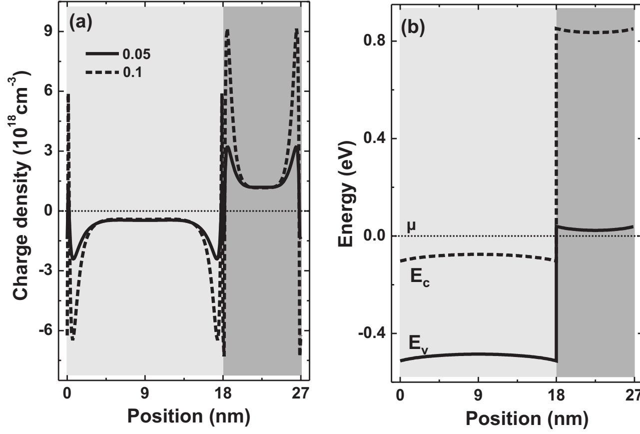

FIG. 5. (a) Calculated local charge density for a wide layer superlattice with 18 and 9 nm for the InAs and GaSb layer width, respectively. The charge density very close to the interface depends on the chosen maximum wave vector $k_\parallel^{\max}$ (full line: 0.05, dashed line: 0.1 in units of $2\pi/a$) in contrast to the charge near the well centers. (b) Calculated electrostatic potential corresponding to (a), superimposed on the bulk conduction (E_C) and valence-band (E_V) edges.

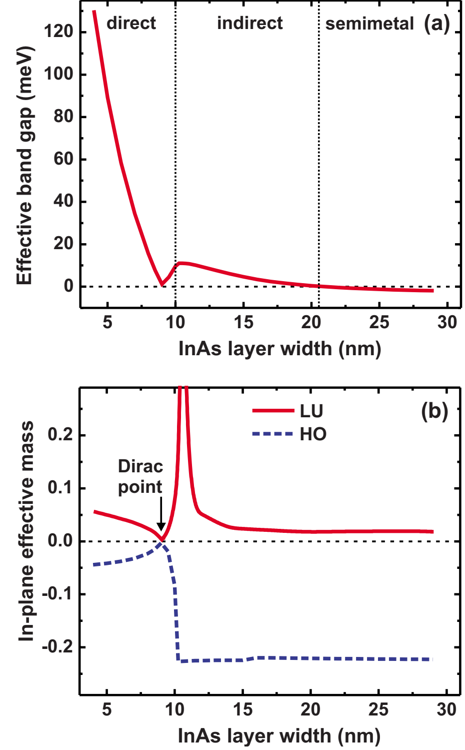

FIG. 6. (Color online) (a) Calculated effective band gap E_G^{eff} of InAs/GaSb superlattices as a function of the InAs layer width for a fixed GaSb layer width of 10 nm. The vertical dotted lines indicate regimes where the band structure corresponds to a direct semiconductor, an indirect semiconductor, and a semimetal, respectively. (b) Calculated in-plane effective masses of LU and HO subband extrema for the same structure. The Dirac point indicates a situation where the in-plane subband dispersion becomes linear.

IV. RESULTS: InAs/GaSb SUPERLATTICES

A. Effective band gap and effective masses

In this section, we present a systematic analysis of the effective band gap and the band-edge effective masses in broken-gap InAs/GaSb superlattices as a function of the well widths. Concretely, we vary the InAs layer widths w_1 from 4 to 30 nm and assume a fixed GaSb layer width of $w_2 = 10$ nm for a temperature of $T=4$ K. The results are summarized in Fig. 6. For the smallest layer widths, strong confinement raises the lowest unoccupied subband (e_0) above the highest occupied subband (h_0) leading to $E_G^{\text{eff}}=E(e_0,\mathbf{k}_\parallel=0)-E(h_0,\mathbf{k}_\parallel=0)>0$ in accordance with Fig. 2(a). With increasing layer width w_1, the reduced confinement leads to a decrease in the effective band gap E_G^{eff}. At $w_1 \approx 9$ nm, E_G^{eff} becomes zero. By further increasing w_1, the subbands e_0 and h_0 swap their energetic positions and an anticrossing gap opens. The effective band gap $E_G^{\text{eff}}=E(h_0,\mathbf{k}_\parallel=0)-E(e_0,\mathbf{k}_\parallel=0)$ remains positive but the HO and LU states have changed. Thus, E_G^{eff} now increases as a consequence of the reduction in confinement. When the InAs layer width is further increased to $w_1 > 10$ nm, we find the extrema of the LU and HO subbands to be located at different values $\mathbf{k}_\parallel^{\text{LU}}$ and $\mathbf{k}_\parallel^{\text{HO}}$ of the in-plane wave vector. Thus, the superlattice becomes an indirect-gap semiconductor, as shown in Fig. 3. By further increasing w_1, the effective gap E_G^{eff} decreases and even becomes negative for $w_1 > 21$ nm. Thus, our results confirm the existence of a semiconductor-semimetal transition that has been predicted before.[12]

In Fig. 6(b), we show the calculated LU and HO in-plane effective masses along the [110] direction. Starting from the smallest layer widths, both LU and HO effective masses decrease in magnitude with increasing InAs layer width. Interestingly, they become zero when the effective band gap vanishes ($w_1 \approx 9$ nm). At this point, our results indicate that the electrons in the InAs/GaSb superlattice layers become a two-dimensional gas of massless Dirac fermions similar to the situation known from graphene.[32] We point out, however, that there are several effects that are not included in the present model that can open a small but finite energy gap. First, the adjacent materials do not share a common atom at the interface which reduces the symmetry and provides a (weak) coupling between LU and HO states.[12] Second, the electron-phonon interaction can resonantly enhance the coupling between the band-edge state similar to the situation in other zero-gap materials.[33]

At the transition from direct to indirect band gaps, the LU mass has a singularity. This corresponds to a flat energy dispersion. For larger values of w_1, this mass tends toward the electron effective mass of bulk InAs ($0.026m_0$). The HO mass, by contrast, stays constant after this transition since this state is dominantly localized within the GaSb layer that has fixed width. We note that the LU and HO masses differ by an order of magnitude from each other in the entire indirect-gap regime.

B. Comparison with experiment

We now turn to a comparison of the present theoretical model with experiments. In the regime of narrow layer

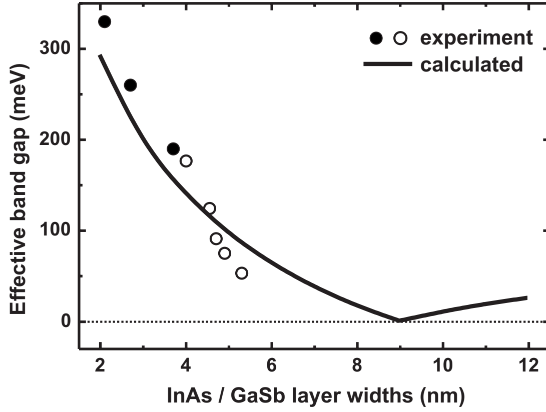

FIG. 7. Calculated effective band gap of InAs/GaSb superlattices of equal individual layer widths, as a function of the layer width. For comparison, we show experimental data from Ref. 18 (full circles) and from Ref. 14 (open circles).

widths, we have calculated the effective band gap E_G^{eff} for superlattices with equal InAs and GaSb layer widths ($w_1 = w_2 = w$). Concretely, we have investigated superlattices with individual layer widths between 2 and 12 nm. The temperature has been set to 4 K. As can be deduced from Fig. 7, our results show good agreement with experimental values.[14,18]

Next, we turn to the regime of wide layer widths. Here, we have calculated transition energies between the HO and LU subbands at $\mathbf{k}_{\parallel}=0$ for superlattices with InAs layer widths w_1 in the range of 10–55 nm and a fixed GaSb layer width of $w_2=10$ nm at $T=4$ K. Our results are shown in Fig. 8 and make it evident that a detailed theoretical model including a consistent coupling of electronlike and holelike states as well as charge-transfer effects is required to realistically interpret and understand experiments. In order to avoid excessive clutter, we only show transition energies in an energy window near the experimental results.[4] We have labeled the HO subbands by e_0, hh_1, lh_0 according to their dominant bulk (electron, light, and heavy hole) character. Similarly the relevant LU states are hh_0, e_1, e_2, e_3. The e states are dominantly localized within the InAs layer, whereas the hh/lh states lie mostly within the GaSb layer. With increasing width w_1, the energies of the e-like states always decrease due to reduction in confinement. In most cases, this implies a decrease in the transition energy except for hh_0-e_0 since hh_0 lies above the chemical potential whereas e_0 lies below it. Interestingly, this transition energy saturates for large layer widths. This effect originates in the charge-transfer-induced band bending [see Fig. 2(b)] that leads to a decrease in the effective energy gap and compensates the reduction in confinement. Note that the h states remain almost constant in energy since we keep the GaSb layer width fixed. Unfortunately, a detailed comparison with experiment is hampered by the fact that the data have been taken at high magnetic fields up to 14 T with the magnetic field lying within the growth plane and extrapolated to zero field. Nevertheless, the data indicate a crossover from the e_1-e_0 transition up to approximately $w=25$ nm to a hh_0-e_0 or e_1-lh_0 transition for the wider InAs wells. Further experiments are needed to clarify the nature of these optical excitations more quantitatively.

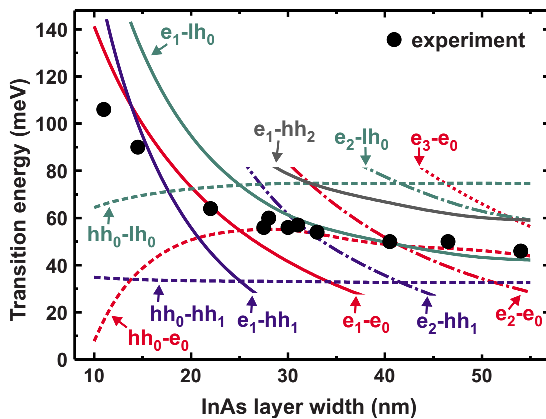

FIG. 8. (Color online) Calculated transition energies between occupied and unoccupied band-edge states of InAs/GaSb superlattices with fixed GaSb layer width of 10 nm, as a function of InAs layer width. The experimental results are from Ref. 4 (circles).

V. SUMMARY

In summary, we have developed a charge self-consistent multiband $\mathbf{k}\cdot\mathbf{p}$ envelope-function method for the calculation of the electronic structure of type-II broken-gap superlattices. When a material has a broken gap, standard multiband $\mathbf{k}\cdot\mathbf{p}$ approaches fail since they depend on an unambiguous separation into electron and hole states. The key point of the presently developed FB-EFA is to remain in the electron framework throughout. In fact, we occupy all included subbands with electrons according to the Fermi statistics and subsequently subtract a positive background ionic charge that guarantees charge neutrality. Importantly, only electronic states of small wave vectors enter the calculation. With this procedure, we have calculated subband dispersions and local charge densities of InAs/GaSb superlattices. The FB-EFA method is equivalent to the standard EFA for conventional type-I semiconductors. For wide layer broken-gap superlattices, the FB-EFA correctly yields the charge transfer between the adjacent material layers. In addition, we have calculated effective band gaps, effective masses, intersubband, and interband transition energies of intrinsic InAs/GaSb superlattices as a function of the layer thickness. We find the charge carriers to approximately form a two-dimensional gas of massless Dirac particles at a critical layer width that is associated with a crossover in the energetic order of the lowest electronlike and the highest holelike subbands. In the regime of wider layer widths, we find a transition from semiconductor to semimetallic regime.

ACKNOWLEDGMENTS

The authors acknowledge support from the Deutsche Forschungsgemeinschaft (Grants No. SFB 631 and No. SPP 1285), the Austrian Science Fund FWF (SFB IRON), and the Nanosystems Initiative Munich (NIM).

[1] J. B. Boos, B. R. Bennett, N. A. Papanicolaou, M. G. Ancona, J. G. Champlain, R. Bass, and B. V. Shanabrook, Electron. Lett. **43**, 834 (2007).
[2] W. Xu, X. F. Wei, and J. Zhang, Appl. Phys. Lett. **92**, 162108 (2008).
[3] R. Ascazubi, I. Wilke, K. J. Kim, and P. Dutta, Phys. Rev. B **74**, 075323 (2006).
[4] A. J. L. Poulter, M. Lakrimi, R. J. Nicholas, N. J. Mason, and P. J. Walker, Phys. Rev. B **59**, 10785 (1999).
[5] E. Halvorsen, Y. Galperin, and K. A. Chao, Phys. Rev. B **61**, 16743 (2000).
[6] H. Ohno, L. Esaki, and E. E. Mendez, Appl. Phys. Lett. **60**, 3153 (1992).
[7] H. Mohseni, E. Michel, J. Sandoen, M. Razeghi, W. Mitchel, and G. Brown, Appl. Phys. Lett. **71**, 1403 (1997).
[8] G. Liu and S.-L. Chuang, Phys. Rev. B **65**, 165220 (2002).
[9] Yu. Vasilyev, S. Suchalkin, K. von Klitzing, B. Meltser, S. Ivanov, and P. Kop'ev, Phys. Rev. B **60**, 10636 (1999).
[10] M. Altarelli, Phys. Rev. B **28**, 842 (1983).
[11] S.-H. Wei and A. Zunger, Phys. Rev. B **52**, 12039 (1995).
[12] R. Magri, L. W. Wang, A. Zunger, I. Vurgaftman, and J. R. Meyer, Phys. Rev. B **61**, 10235 (2000).
[13] P. Piquini, A. Zunger, and R. Magri, Phys. Rev. B **77**, 115314 (2008).
[14] Y. Wei and M. Razeghi, Phys. Rev. B **69**, 085316 (2004).
[15] W. Xu, P. A. Folkes, and G. Gumps, J. Appl. Phys. **102**, 033703 (2007).
[16] I. Lapushkin, A. Zakharova, S. T. Yen, and K. A. Chao, J. Phys.: Condens. Matter **16**, 4677 (2004).
[17] I. Semenikhin, A. Zakharova, and K. A. Chao, Phys. Rev. B **77**, 113307 (2008).
[18] L. L. Chang, G. A. Sai-Halasz, L. Esaki, and R. L. Aggarwal, J. Vac. Sci. Technol. **19**, 589 (1981).
[19] J. M. Luttinger and W. Kohn, Phys. Rev. **97**, 869 (1955).
[20] G. Bastard, Phys. Rev. B **24**, 5693 (1981).
[21] M. G. Burt, J. Phys.: Condens. Matter **11**, R53 (1999).
[22] B. A. Foreman, Phys. Rev. B **56**, R12748 (1997).
[23] T. Andlauer, R. Morschl, and P. Vogl, Phys. Rev. B **78**, 075317 (2008).
[24] See http://www.wsi.tum.de/nextnano for obtaining the NEXTNANO executables and related publications.
[25] I. Vurgaftman, J. R. Meyer, and L. R. Ram-Mohan, J. Appl. Phys. **89**, 5815 (2001).
[26] S. L. Cunningham, Phys. Rev. B **10**, 4988 (1974).
[27] J. F. Cooke and R. F. Wood, Phys. Rev. B **5**, 1276 (1972).
[28] G. Wiesenekker, G. te Velde, and E. J. Baerends, J. Phys. C **21**, 4263 (1988).
[29] W. H. Press, S. A. Teukolsky, W. T. Vetterling, and B. P. Flannery, *Numerical Recipes in Fortran 90* (Cambridge University Press, Cambridge, U.K., 1996).
[30] A. Baldereschi, S. Baroni, and R. Resta, Phys. Rev. Lett. **61**, 734 (1988).
[31] S.-H. Wei and A. Zunger, Appl. Phys. Lett. **72**, 2011 (1998).
[32] K. S. Novoselov, A. K. Geim, S. V. Morozov, D. Jiang, M. I. Katsnelson, I. V. Grigorieva, S. V. Dubonos, and A. A. Firsov, Nature (London) **438**, 197 (2005).
[33] E. M. Sheregii, J. Cebulski, A. Marcelli, and M. Piccinini, Phys. Rev. Lett. **102**, 045504 (2009).